



## Experimental Evaluation of a 3-Armed 6-DOF Parallel Robot for Femur Fracture Surgery

Fayez Alruwaili\*, Marzieh S. Saeedi-Hosseiny†, Michael Clancy\*,  
Sean McMillan‡, Julian I. Iordachita§, Mohammad H. Abedin-Nasab\*¶

\*Biomedical Engineering, Rowan University, 201 Mullica Hill Rd Glassboro, NJ 08028, USA

†Electrical and Computer Engineering, Rowan University, 201 Mullica Hill Rd  
Glassboro, NJ 08028, USA

‡School of Osteopathic Medicine, Rowan University, 113 E Laurel Rd  
Stratford, NJ 08084, USA

§Laboratory for Computational Sensing and Robotics  
Johns Hopkins University, 3400 N Charles St, Baltimore, MD 21218, USA

This paper presents the experimental position and force testing of a 3-armed 6-DOF Parallel Robot, Robossis, that is specifically designed for the application of long-bone femur fracture surgery. Current surgical techniques require a significant amount of time and effort to restore the fractured femur fragments' length, alignment and rotation. To address these issues, the Robossis system will facilitate the femur fracture surgical procedure and oppose the large traction forces/torques of the muscle groups surrounding the femur. As such, Robossis would subsequently improve patient outcomes by eliminating intraoperative injuries, reducing radiation exposure from X-rays during surgery and decreasing the likelihood of follow-up operations. Specifically, in this paper, we study the accuracy of the Robossis system while moving in the operational workspace under free and simulated traction loads of (~ 50–1100 N). Experimental testing in this study demonstrates that Robossis can reach the most extreme points in the workspace, as defined by the theoretical workspace, while maintaining minimal deviation from those points with an average deviation of 0.324 mm. Furthermore, the force testing experiment shows that Robossis can counteract loads that are clinically relevant to restoring the fractured femur fragments' length, alignment and rotation. In addition, we study the accuracy of Robossis motion while coupled with the master controller Sigma 7. The results show that Robossis can follow the desired trajectory in real-time with an average error of less than 1 mm. To conclude, these results further establish the ability of the Robossis system to facilitate the femur fracture surgical procedure and eliminate limitations faced with the current surgical techniques.

**Keywords:** Robot-assisted surgery; femur fractures; parallel mechanism; Robossis.



### 1. Introduction

Surgical robotics has surged into the spotlight of surgical technology in the last 40 years due to the demand for

Received 31 July 2022; Revised 5 October 2022; Accepted 22 October 2022; Published 9 December 2022. Published in JMRR Special Issue on International Symposium on Medical Robotics (ISMР 2022). Guest Editor: Elena De Momi.

Email Address: [tabedin@rowan.edu](mailto:tabedin@rowan.edu)

NOTICE: Prior to using any material contained in this paper, the users are advised to consult with the individual paper author(s) regarding the material contained in this paper, including but not limited to, their specific design(s) and recommendation(s).

increased speed and accuracy needed for the evolution of healthcare [1–4]. The rise in fractures since the early 2000s [5,6] has led to extensive research and studies conducted on robots specifically designed for fracture alignment surgeries [7,8]. Long-bone fractures have been of particular interest for robot-assisted surgeries due to the limitation of current methods, including the substantial amount of force required to reposition and fixate the fragments, the high rates of malalignment and mal-rotation, and the elongated X-ray exposure to the operating staff [7–10].

Although robot-assisted surgeries have been studied for years, there has not been a properly designed system that can handle the complex extremities of long-bone fracture fixation, including the need for immense forces/torques competence (517 N and 74 N·m, respectively), pinpoint accuracy and the large operational robot translation and rotational workspace (Table 1). To address these extremities faced during long-bone fracture surgeries, our group has presented a novel design of a 3-armed 6-DOF parallel robot, Robossis, theoretical analysis [11–15], preliminary experimental force and position testing [16] and cadaveric experiment [17].

Furthermore, in this study, we present more extensive experimental force and position testing for the Robossis system. Specifically, we study the accuracy of the Robossis system while moving in the operational workspace with free and varying loads applied to the structure. We model the forces as springs with loads increasing to 1100 N. In addition, we study the accuracy of Robossis motion coupled with the master controller (Sigma-7, Force Dimension – Switzerland).

This paper is organized as follows. Section 2 presents the clinical challenges and requirements for femur fracture surgery. Section 3 presents the Robossis system architecture. Section 4 presents the experimental testing, including workspace, movement in a straight line, load insertion, and real-time motion via the master controller. Finally, Sec. 5 presents the discussion, and Sec. 6 concludes.

## 2. Clinical Challenges and Requirements

A surgical robot developed for the application of long-bone femur fracture surgery must be designed to meet

the clinical requirement. The required accuracy for the alignment of the long-bone femur fracture is defined based on the Thoresen scoring system [44],  $\pm 1$  cm and  $\pm 5^\circ$  for translational and rotational alignment, respectively. Malrotation is one of the most significant complications of femur fracture surgery (Table 2). Table 2 shows that the outcome of current surgical techniques to treat long-bone femur fractures results in a high rate of malrotation, which alters the patient's gait mechanics and efficiency [45,46].

Furthermore, the long-bone femur is surrounded by the largest muscle groups in the human body, which require large traction forces/torques during the surgical operation. As such, manipulation of the fractured femur fragments is very difficult and requires the extensive clinical expertise of multiple doctors. Previous studies [52,53] have defined the traction forces/torques requirements during femur fracture surgery. Based on the anatomical [52,53] medial-lateral axis, the anterior-posterior axis, and the femoral shaft axis, the maximum forces required were defined as 202, 517 and 505 N, respectively. In addition, the maximum torques required in the medial-lateral axis, the anterior-posterior axis, and the femoral shaft axis were defined as 16.4, 38.3 and 74 N·m, respectively.

Additionally, the required rotational and translational workspaces for a robotic system designed for long-bone femur fracture surgery can be deducted based on the previously reported literature on post-operative mal-rotation and shorting of the leg [51,54,55]. We provide a quantitative approximation for the desired workspace limits in the femoral shaft axis in Table 3. This approximation is based on the maximal shortening and mal-rotation along the femoral shaft axis observed in

**Table 1.** Robot-assisted systems for femur fractures. Gough–Stewart platform (GSP), Serial (S), Parallel (P), Hybrid (H) and Not Reported (NR).

| Year of research | Mechanism type          | Subject study    | Max load force (N) |
|------------------|-------------------------|------------------|--------------------|
| 1995 [18]        | S                       | Bone model       | 50                 |
| 2004 [19]        | S, Stäubli RX130        | Bone model       | 240                |
| 2004 [20]        | P, GSP                  | Human model      | NR                 |
| 2006 [21]        | S, Stäubli RX90         | Human cadaver    | < 300              |
| 2008 [22]        | S, Stäubli RX90         | Rat model        | 250                |
| 2009 [23]        | S, Stäubli RX90         | Bone model       | < 300              |
| 2010 [24]        | S, Stäubli RX90         | Human cadaver    | < 300              |
| 2012 [25–27]     | S-P-H                   | Position testing | 600                |
| 2013 [28,29]     | P, GSP                  | Bovine femoral   | NR                 |
| 2013 [30]        | P, GSP                  | Human cadaver    | NR                 |
| 2014 [31]        | P, GSP                  | Bone model       | 2460               |
| 2017 [32–35]     | P, GSP                  | Bovine bone      | 1243               |
| 2016 [36–39]     | S-P-H                   | Human cadaver    | < 300              |
| 2020 [40]        | P, GSP                  | Bone model       | NR                 |
| 2022 [41]        | P, GSP                  | Bone model       | 500                |
| 2022 [42]        | P, GSP                  | Animal model     | 561                |
| 2022 [43]        | Serial + Traction Table | Bone model       | 158                |

**Table 2.** Malrotation of the proximal (P), shaft (S) and distal (D) femur occurs at a high rate after surgical operation.

| Study type | Study sample size | Malrotation rate | Malrotation definition |
|------------|-------------------|------------------|------------------------|
| S [9]      | 530               | 28%              | $\geq 10^\circ$        |
| P [47]     | 70                | 24%              | $\geq 10^\circ$        |
| S [48]     | 76                | 28%              | $\geq 15^\circ$        |
| D [49]     | 51                | 27%              | $\geq 12^\circ$        |
| S [50]     | 24                | 41%              | $\geq 10^\circ$        |
| S [51]     | 24                | 41%              | $\geq 15^\circ$        |

**Table 3.** Major clinical requirements for a designed robot-assisted surgery system for the application of long-bone femur fracture.

| Parameter   | Clinical requirement                   |
|---|--|
| Accuracy [44]   | $\pm 1 \text{ cm}, \pm 5^\circ$        |
| Loads [52,53]   | 517 N, 74 N*m                          |
| Trans and Rot Workspace (femoral shaft axis) [51,54,55] | $\pm 5.4 \text{ cm}$<br>$\pm 40^\circ$ |

the literature. As such, a designed system for femur surgery must meet the desired accuracy, load insertion and workspace requirements to manipulate the long-bone femur fracture.

### 3. Robossis System Architecture

Robossis system is designed based on a 3-armed parallel mechanism where each arm is placed on a moving and fixed ring (Fig. 1). The Robossis system is designed to meet the clinical requirements of femur fracture surgery which includes (1) adequately applying the large traction forces/torques, (2) precisely aligning the fractured bone and (3) manipulating the distal bone fragment during the surgical procedure. Each arm of the Robossis includes three joints: Universal, prismatic and spherical (Fig. 1). The universal joint connects the rotary actuator shaft to the lower arm and is fixed on a semicircle to the fixed platform. In addition, the spherical joints connect the upper parts of the linear actuators to the moving ring.

To satisfy the needs of the necessary load insertion during femur fracture surgery, Robossis actuators are selected. A 260 W Autonics-A8K stepper motor with a nominal torque of 0.83 Nm powers the rotary actuator. The Autonics-A8K is also coupled with an Apex 60:1 gearbox, raising the maximum holding torque to 48.6 Nm for a total of 145.8 Nm. A revolute joint formed from a needle bearing joins the gearbox shaft to the lower part of the arm. Each arm includes a linear actuator of a Hiwin KK40 linear guide with a 1.0 mm pitch. Each linear actuator is powered via an 80 W Autonics-A3K stepper motor with a nominal torque of 0.24 Nm, resulting in a maximum insertable linear force of 1527 N at each arm.

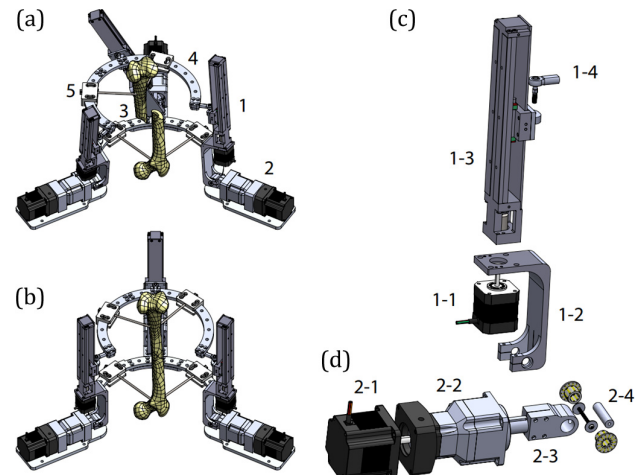


**Fig. 1.** (a) Robossis mechanism [17] consists of three arms (1-2) where each arm is attached to (3) a fixed ring, and (4) a moving ring. The bone is attached to the patient using surgical rods (5). (b) The Robossis mechanism after manipulation of the fractured bone to demonstrate the various joints movement on bone manipulation. Each arm of Robossis (c-d) is equipped with an Autonics-A3K stepper motor (1-1), (1-2) Hiwin KK40 linear guide (1-3) and spherical joint (1-4), Autonics-A8K actuator (2-1), Apex 60:1 gearbox (2-2), universal joint (2-3) and roller bearing and thrust roller bearing (2-4).

Therefore, using the A3K micro-stepper in the proposed system, Robossis can theoretically insert up to 4559 N.

#### 3.1. Inverse kinematics analysis

The inverse kinematics of the Robossis system was developed to maneuver the endpoint effector (Fig. 2) [11-14].

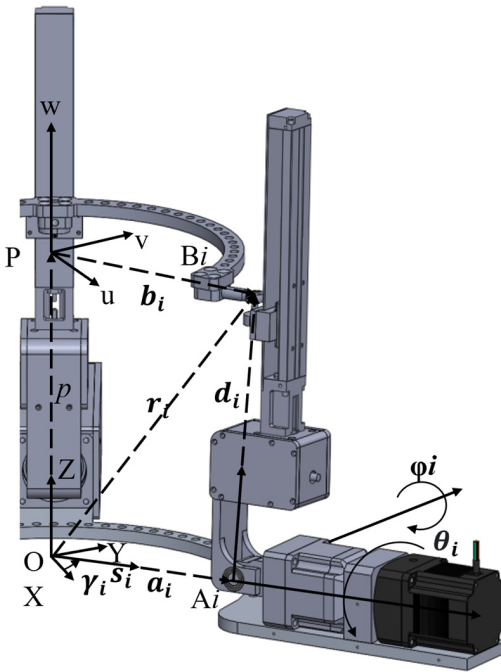


**Fig. 2.** Kinematic variables of the  $i$ th arm are shown.  $\theta_i$  is the active rotation, followed by the passive  $\psi_i$  rotation.

Given the desired position and orientation of the end-point effector (P), the required length of the linear actuator ( $d_i$ ) and the rotation of the active joint ( $\theta_i$ ) are computed. Referring to Fig. 2,  $a_i$  and  $b_i$  represents  $O A_i$ , and  $P B_i$ , respectively. Denoting  $r_i$  and  $p$  as a position vector  $[x \ y \ z]^T$  in frame  $\{A\}$ , it can be concluded from the structure that

$$r_i - a_i = p + b_i - a_i, \quad (1)$$

where the left-hand side is the length vector of the linear actuator ( $d_i$ ), simplifying and using Euclidean norm,  $d_i$  can be expressed as

$$d_i = \sqrt{(x - x_i)^2 + (y - y_i)^2 + (z - z_i)^2}. \quad (2)$$

Also, the active joint ( $\theta_i$ ) is expressed as shown in the following equation:

$$\theta_i = \sin^{-1} \left( \frac{\sin(\gamma_i) * (x - x_i) - \cos(\gamma_i) * (y - y_i)}{d_i \cos(\psi_i)} \right), \quad (3)$$

where  $\gamma_i$  is the  $i$ th location of each arm, and  $\psi_i$  is the angle of the passive joint ( $i = 1, 2, 3$ ).

### 3.2. Trajectory generation

Trajectory generation of the Robossis system can be achieved with a manual or real-time motion via the master controller. For manual control, a time-controlled trajectory generation scheme is implemented using a

trigonometric function:

$$x(t) = \begin{cases} x_0, & t < t_0 \\ x_0 + dx, & t > t_0 + dt \\ \frac{dx}{2} * \sin \left( \frac{180}{dt} * (t - t_0) - 90 \right) \\ + x_0 + \frac{dx}{2} & \end{cases}, \quad (4)$$

where  $x_0$  is the initial position,  $dx$  is the desired change of motion,  $t_0$  is the initial time of change and  $dt$  is the desired time to complete the motion. The time-controlled trajectory scheme is generalized to all translational and rotational motions.

Furthermore, real-time motion of Robossis was coupled with the master controller with a trajectory generation scheme using splines and control via waypoints (Fig. 3). A cubic spline  $S_{3,n}(t)$  is a piecewise cubic polynomial and mathematically defined by four coefficients,  $a_{3,n}, b_{3,n}, c_{3,n}$  and  $d_{3,n}$  as follows:

$$S_{3,n} = \begin{bmatrix} d_{3,0}(t)^3 + c_{3,0}(t)^2 + b_{3,0}(t) + a_{3,0} \in [t_0 \ t_1] \\ d_{3,1}(t)^3 + c_{3,1}(t)^2 + b_{3,1}(t) + a_{3,1} \in [t_1 \ t_2] \\ \vdots \\ d_{3,n}(t)^3 + c_{3,n}(t)^2 + b_{3,n}(t) + a_{3,n} \in [t_{n-1} \ t_n] \end{bmatrix}, \quad (5)$$

where  $a_{3,n}, b_{3,n}, c_{3,n}$  and  $d_{3,n}$  are solved using the conventional clamped cubic spline algorithm [56]. Furthermore, the velocity at each piecewise cubic polynomial can be estimated as follows:

$$S_{3,n}(t)' = 3d_{3,n}(t)^2 + 2c_{3,n}(t) + b_{3,n} \in [t_{n-1} \ t_n]. \quad (6)$$

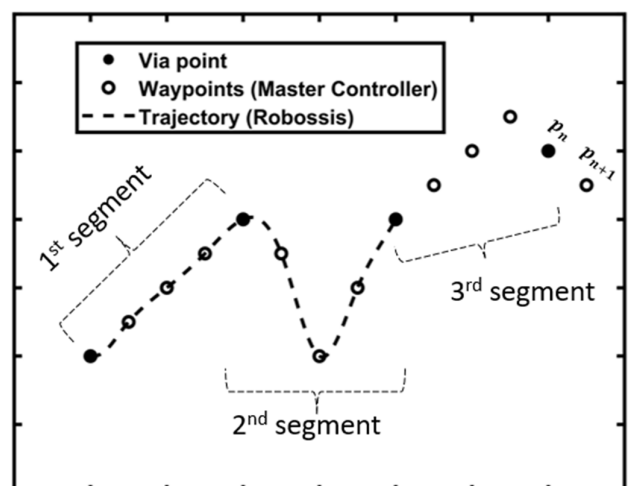


**Fig. 3.** A trajectory generation scheme implemented to couple the motion of the master controller at real-time. Via points are used to connect the waypoints and the segments of the trajectory.

Using the clamped cubic spline, a third-order continuity for the position, velocity and acceleration is ensured through each segment of the trajectory, and a maximum of four boundary conditions must be specified (i.e. initial and final position and velocities) for each trajectory segment.

We implement via control points to connect the clamped cubic spline's trajectory segments to extend the trajectory to a real-time motion. Constraints are imposed on the via points to obtain a smooth trajectory which includes a velocity constraint. The velocity at the via point is estimated using the central differential method as follows:

$$V_{\text{via}} = \left( \frac{p_{n+1} - p_n}{t_{n+1} - t_n} + \frac{p_n - p_{n-1}}{t_n - t_{n-1}} \right) * \frac{1}{2}. \quad (7)$$

As such, motion coupling of the master controller with Robossis is achieved with the trajectory generation scheme.

#### 4. Experimental Testing

Experimental testing of the Robossis system is conducted to study the accuracy and load insertion capability. The Robossis system is manufactured using computer

numerical control (CNC) (frame material: Al 6061) machining and assembled as shown in Fig. 4(a). The mechanism consists of (1) a fixed ring, (2) a moving ring, (3) linear actuators and (4) rotary actuators. Also, (5) shows that the rings are attached to the fractured bone through half-pin rods. Figure 4(b) presents the compact workstation of the Robossis system, which includes (1) a touch screen control panel and (2) the 7-DOF haptic Sigma-7 master controller. Additionally, Fig. 4(c) shows the control panel of the Robossis system, where the user can switch between the manual and real-time master controller motion. The control panel allows the user to lock the movement of the master controller to any desired direction and adjust the speed of the motion.

Furthermore, the performance of Robossis was determined through multiple experimental testing procedures, including workspace, movement in a straight line, load insertion and real-time motion via the master controller. These preliminary testing procedures were conducted to determine the ability of Robossis to be successful in aligning and restoring the length of the femur fragments in the clinical setting.

Also, we implement the Euclidean distance between the actual (A) and theoretical (Th) values as the error metric for analysis in this study.

$$\text{Error} = \sqrt{|X_A - X_{Th}|^2 + |Y_A - Y_{Th}|^2 + |Z_A - Z_{Th}|^2}. \quad (8)$$

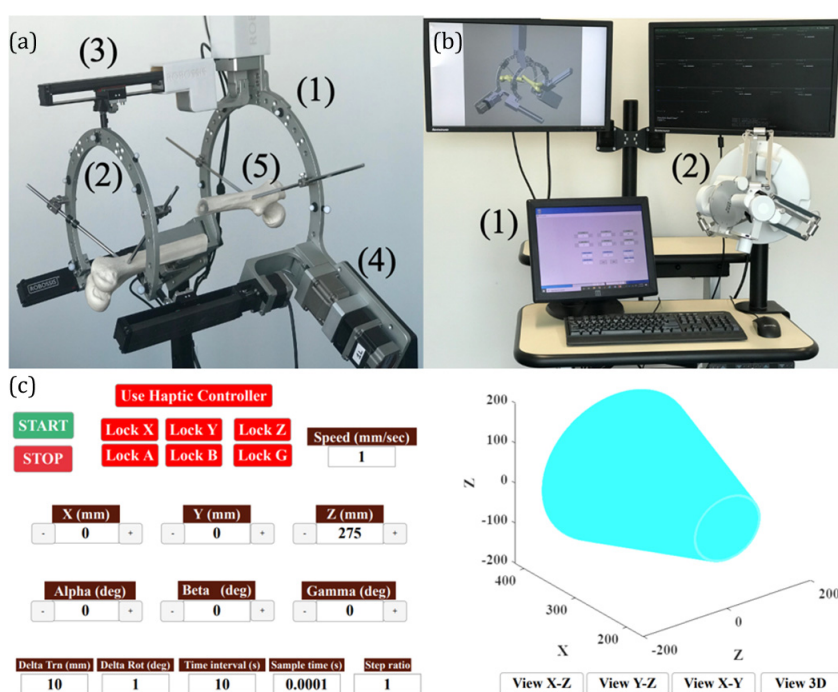


**Fig. 4.** (a) The fully assembled Robossis system. The mechanism consists of a (1) fixed ring, (2) moving ring, (3) linear actuator and (4) rotary actuator. The rings are attached to the fractured bone through half-pin rods (5). (b) workstation which include (1) touch screen control panel, (2) 7 DOF sigma-7 master controller and screen monitors for real-time feedback on the performance of the robot. (c) the control panel of the Robossis system where the user can switch between the manual and real-time master controller motion.

#### 4.1. Workspace testing

Workspace testing of Robossis is completed to determine the system's accuracy in moving to different locations in the operational workspace. During testing, Robossis was tasked to move to locations in the operational workspace for every  $5^\circ$  and increased height and radius by 10 mm and 3 mm, respectively. The motion of Robossis was coupled with an optical tracking system (Optitrack Flex 13, residual within 0.5 mm, NaturalPoint, Inc. DPA Opti-Track) to determine the accuracy of Robossis in reaching these locations. The results of the workspace testing shown in Fig. 5 illustrate that Robossis can reach the most extreme points in the workspace while maintaining minimal deviation from those points. Furthermore, the box plot shown in Fig. 5 illustrates that the deviation in the workspace testing had an average and maximum Euclidean error of 0.324 and 3.84 (mm), respectively.

#### 4.2. Load insertion

The femur is surrounded by the strongest muscle groups, which require large traction forces/torques during surgical manipulation. As such, to simulate the muscle traction forces and determine Robossis load insertion ability, a preliminary force testing rig was developed with three force gauges (WeiHeng Mini Portable Electronic Scale, capacity = 1471 N) and three springs (Fig. 6). The force testing rig is depicted in Fig. 6 where the springs and force gauges were connected to the proximal and distal half-pins of Robossis moving and fixed rings.

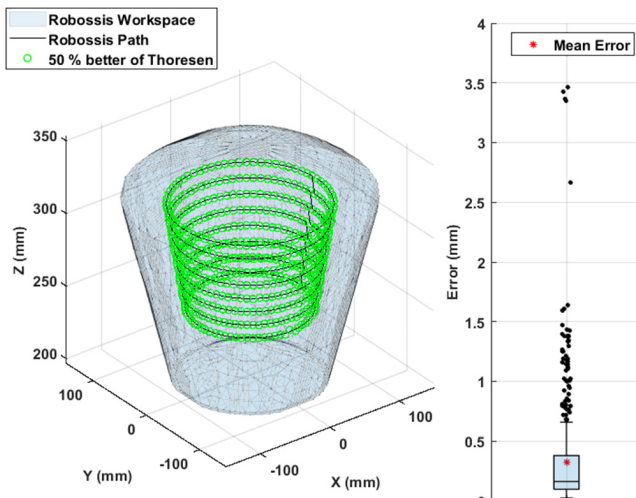


**Fig. 5.** Experimental testing of the workspace presented as the Euclidean error between the desired and measured locations read by the Optitrack system. The green coloring indicates that each marker exceeded the clinical requirement of at least 50% better than the Thoresen metric. Also, the box plot shows an average and maximum Euclidean error of 0.324 (mm) and 3.84 (mm), respectively.



**Fig. 6.** The force testing benchtop model includes three force gauges (1) and three springs (2). Also, the force gauges and springs were attached to Robossis moving and fixed rings.

The testing procedure tasked Robossis to move in an increment and extend the springs to their maximum resistive force. During this test procedure, the benchtop model was able to generate a resistive force of  $\sim 1100$  N and Robossis was able to withstand this resistive force, as shown in Fig. 7. As such, Robossis is able to insert two times more than the required traction forces as reported in the literature.

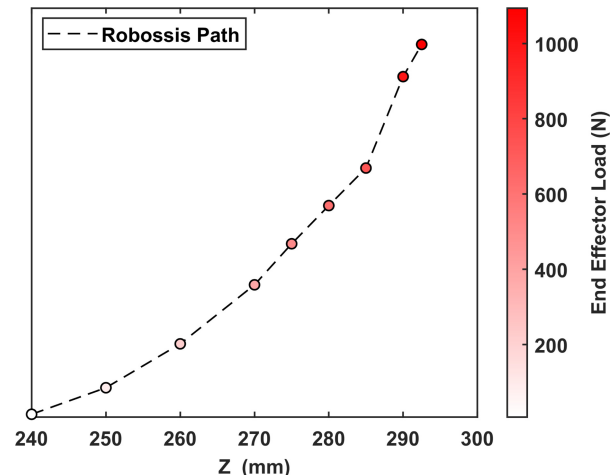


**Fig. 7.** Robossis was tasked to move in an increment and extend the springs to their maximum resistive force ( $\sim 1100$  N). As such, Robossis is able to insert two times more than the required traction forces as reported in the literature.

#### 4.3. Straight line testing

A movement in a straight-line testing procedure was conducted to further investigate the accuracy of Robossis while experiencing external forces. A testing procedure was completed where Robossis was tasked to follow a square path of 160 mm by 160 mm. The optical tracking system measured the location of the endpoint effector along the path to determine the accuracy throughout the testing procedure. Two different testing setups were implemented to introduce varying stresses on the frame of Robossis during movement. (1) No external loads and (2) external loads in the form of springs and force sensors to simulate passive muscle traction forces. The results show that the Robossis mechanism meets the clinical requirement of 50% better than the “excellent” Thoresen metric parameter both without external loads and with loads up to  $\sim 600$  N of force (Fig. 8).

#### 4.4. Motion via master controller

Real-time motion testing of Robossis is completed to determine the system’s accuracy when moving to different locations in the operational workspace. During testing, Robossis was tasked to follow the motion of the

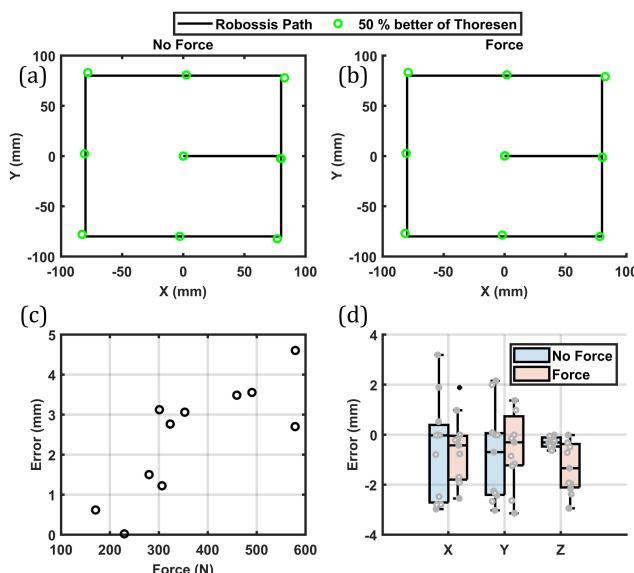


**Fig. 8.** (a) and (b) Straight line movement testing is presented as the comparison of Robossis while moving with and without external force. The results show that the Robossis mechanism performs 50% better than the Thoresen metric both with and without external load. (c) Euclidean error vs. the inserted force presents a correlation determination ( $r^2$ ) value of 0.6. (d) The box plot shows a maximum mean absolute error of 1.33 mm in the z-direction while moving with loads. Also, a maximum absolute error of 3.14 mm is observed in the y-direction while moving with loads.

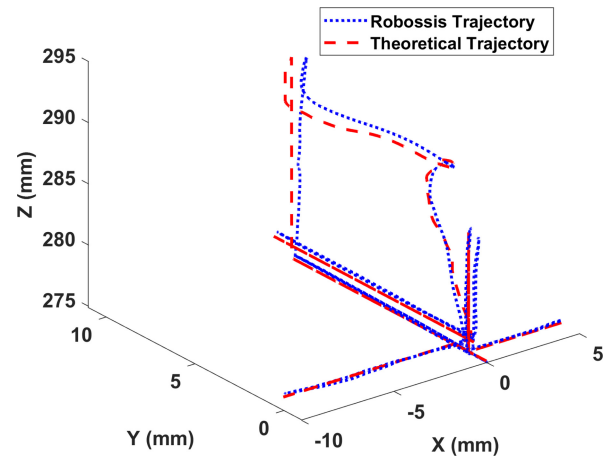


**Fig. 9.** Robossis is able to follow the motion of the user’s hand at real-time using the trajectory generation scheme. The error analysis shows an average error of less than 1 mm between Robossis system and the user’s hand desired trajectory.

user’s hands at real-time in the operational workspace, and we determined the error of the motion.

The results in Fig. 9 show that Robossis can follow the desired trajectory of the user’s hand in real-time using the trajectory generation scheme implemented using splines. The error analysis shows an average error of less than 1 mm between the Robossis system and the user’s hand desired trajectory. Furthermore, Fig. 10 shows a comparison between the trajectory of the user’s hand (via the master controller), theoretical trajectory and actual trajectory (Robossis) for all X, Y and Z directions. The analysis shows that the absolute error in each

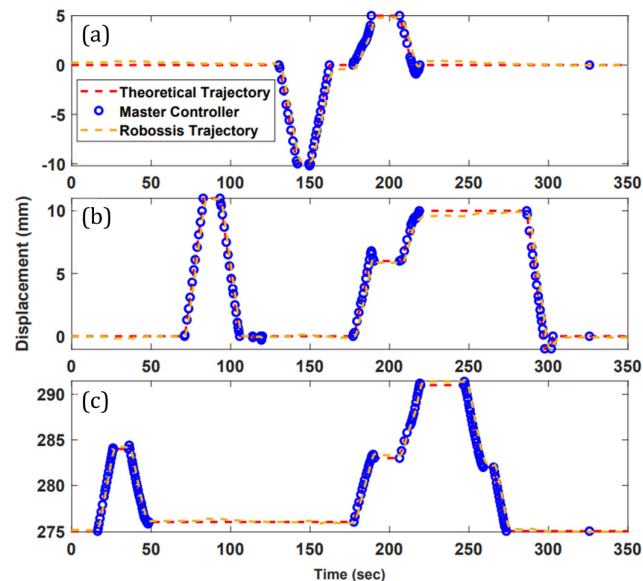


**Fig. 10.** Comparison between trajectory of the user hand (via the master controller), theoretical trajectory and actual trajectory (Robossis) for all X (A), Y (B) and Z (C) directions.

direction was less than 1 mm, and there was no overshoot observed in the trajectories.

## 5. Discussion

The experimental position and force testing conducted in this study, and previous studies completed by our group, including the theoretical analysis [11–15], preliminary experimental force and position testing [16] and cadaveric experiment [17] further reinforce the advantages of the Robossis system as compared to the current state-of-the-art surgical techniques and previous attempts of robotic development (Table 1). The Robossis system is designed to meet the clinical requirements of femur fracture surgery which include (1) Sufficient forces and torques to overcome the passive muscle forces, (2) precisely aligning the fractured bone and (3) manipulating the distal bone fragment during the surgical procedure.

As compared to the previous robotic development, the Robossis mechanism has the advantage of meeting the required loads for the long-bone femur fracture ( $\sim 517$  N), the required accuracy following the Thoresen metric, and the required operational workspaces in the femur shaft axis ( $\pm 50^\circ$  and  $\pm 70$  mm). Creating a robot-assisted system using the Gough–Stewart Platform architecture has resulted in limited rotations around the femoral shaft axis. ( $\pm 17^\circ$  [28,29]). Also, serial robots have not been shown to generate the required forces/torques ( $< 300$  N). The limitations of traditional serial and parallel mechanisms will prevent the patient from being positioned at the surgeon’s discretion, leading to higher risks of patient injury, further surgical complications and malalignment-related complications.

Furthermore, Essomba and Nguyen Phu [40] presented a novel alternation of the Gough–Stewart platform and the design of its components for the application of long-bone fracture surgery. Theoretical analysis of their proposed mechanism presented unique properties where it showed that the mechanism could achieve  $\pm 180^\circ$  rotation around the femoral shaft axis. However, their experimental testing was based on preliminary bone testing, and the feasibility of the system in the clinical setting has not been demonstrated yet [40].

In the same vein, the workspace and straight-line testing demonstrate the accuracy of Robossis movement in the operational workspace as desired by the theoretical values. Furthermore, it shows the reliability of the control software and its inverse kinematics model to deliver the proper joint velocities to move Robossis precisely in a six-dimensional space. Additionally, the real-time motion study shows that Robossis is able to follow the motion of the user’s hand and maintains a high level of accuracy over numerous movements with an average error of less than 1 mm.

Furthermore, the load insertion tests show that Robossis can deliver the required loads that are clinically relevant to restoring the length, alignment and rotation of the fractured femur fragments. As we were able to deliver traction forces of  $\sim 1100$  N along the femoral shaft axis, this study reinforces the advantage of the Robossis system for femur fracture surgeries. For future studies, it would be prudent to reconsider animal models rather than springs to determine the specific spatial accuracy under large loads. Additionally, it would be prudent to consider a closed-loop control mechanism to account for some of the errors due to joint clearances.

Overall, previous studies completed by our group, including the theoretical analysis [11–15], preliminary experimental force and position testing [16], cadaveric experiment [17] and the current study form the basis for a complete robot-assisted system for the application of femur fracture surgery. In learning the current abilities and limitations of Robossis, we seek to implement the discussed improvements in the robotic design to prepare for additional cadaveric and clinical experiments. Such experiment will be beneficial in uncovering any further limitations for applications of the proposed robot and workflow that have not been discussed in this paper.

## 6. Conclusion

To successfully restore the length, alignment and rotation of the fractured femur fragments, the femur fragments must be manipulated and returned to their correct anatomical position. All of this must be done while the surgeon is exerting a large traction force ( $\sim 517$  N). In this study, we have been able to successfully present the experimental position and force testing for a 6-DOF 3-armed parallel robot that is designed to reduce and manipulate the femur fractured fragments by applying the needed traction forces that counteract the muscle payload surrounding the human femur.

The feasibility of the system was experimentally evaluated through the testing of the workspace, movement in a straight line, load insertion and real-time motion via the master controller. Through experimental testing, Robossis system has the potential to be used clinically in order to improve the quality of fracture reduction and realignment with no need for repetitive manipulations and a high amount of radiation exposure to the operating staff and patients.

## Acknowledgments

This research is partially funded by the National Science Foundation (NSF) under Grant No. 2005570 and by the

New Jersey Health Foundation (NJHF) under Grant PC 62-21.

## References

- P. Gomes, Surgical robotics: Reviewing the past, analysing the present, imagining the future, *Robot Comput. Integrat. Manuf.* **27**(2) (2011) 261–266, doi: 10.1016/j.rcim.2010.06.009.
- K. Huang, D. Chitrakar, W. Jiang, I. Yung and Y.-H. Su, Surgical tool segmentation with pose-informed morphological polar transform of endoscopic images, *J. Med. Robot. Res.* **7**(2–3) (2022) 2241003.
- F. King *et al.*, An immersive virtual reality environment for diagnostic imaging, *J. Med. Robot. Res.* **1**(01) (2016) 1640003.
- M. Musa, S. Sengupta and Y. Chen, Design of a 6 DoF parallel robotic platform for MRI applications, *J. Med. Robot. Res.* **7**(2–3) (2022) 2241005.
- T. Meling, K. Harboe and K. Søreide, Incidence of traumatic long-bone fractures requiring in-hospital management: A prospective age- and gender-specific analysis of 4890 fractures, *Injury* **40**(11) (2009) 1212–1219, doi: 10.1016/j.injury.2009.06.003.
- C. M. Court-Brown and B. Caesar, Epidemiology of adult fractures: A review, *Injury*, **37**(8) (2006) 691–697, doi: 10.1016/j.injury.2006.04.130.
- J. X. Zhao, C. Li, H. Ren, M. Hao, L. C. Zhang and P. F. Tang, Evolution and current applications of robot-assisted fracture reduction: A comprehensive review, *Ann. Biomed. Eng.* **48**(1) (2020) 203–224, doi: 10.1007/s10439-019-02332-y.
- L. Bai, J. Yang, X. Chen, Y. Sun and X. Li, Medical robotics in bone fracture reduction surgery: A review, *Sensors (Switzerland)* **19**(16) (2019) 3593, doi: 10.3390/s19163593.
- B. Michael Wesley Honeycutt, K. Cox, W. T. Cox, M. Gregg Delgado and J. Brewer, The effect of intramedullary nail entry point on postoperative femoral shaft.pdf. University of South Alabama, Mobile, AL, United States, 2019. Available at <https://ota.org/sites/files/abstracts/2019/OTA AM19 Paper 100.pdf>.
- Z. H. Birner, S. J. Hetzel, N. M. Wilson and P. S. Whiting, Radiographic outcomes of femur fractures following SIGN Fin nailing in low- and middle-income countries, *OTA Int.* **4**(3) (2021) e141, doi: 10.1097/oi9.00000000000000141.
- M. H. Abedinnasab and G. R. Vossoughi, Analysis of a 6-DOF redundantly actuated 4-legged parallel mechanism, *Nonlinear Dyn.* **58**(4) (2009) 611–622, doi: 10.1007/s11071-009-9504-1.
- M. H. Abedinnasab, Y.-J. Yoon and H. Zohoor, Exploiting higher kinematic performance-using a 4-legged redundant PM rather than Gough-Stewart platforms, *Serial Parallel Robot Manipulators-Kinematics Dyn. Control Optimiz.* **10** (2012) 32141.
- M. H. Abedinnasab, J. G. Alvarado, B. Tarvirdizadeh and F. Farahmand, Sliding-mode tracking control of the 6-dof 3-legged wide-open parallel robot, in *Parallel Manipulators: Design, Applications and Dynamic Analysis* (Nova Science Publishers, Inc., 2016), pp. 143–166.
- M. H. Abedinnasab, F. Farahmand, B. Tarvirdizadeh, H. Zohoor and J. Gallardo-Alvarado, Kinematic effects of number of legs in 6-DOF UPS parallel mechanisms, *Robotica* **35**(12) (2017) 2257–2277, doi: 10.1017/S0263574716000862.
- M. S. Saeedi-Hosseiny, F. Alruwaili, A. S. Patel, S. McMillan, I. I. Iordachita and M. H. Abedin-Nasab, Spatial detection of the shafts of fractured femur for image-guided robotic surgery, *IEEE Eng. Med. Biol. Soc.* (2021).
- F. Alruwaili, M. S. Saeedi-Hosseiny, L. Guzman, S. McMillan, I. I. Iordachita and M. H. Abedin-Nasab, A 3-Armed 6-DOF parallel robot for femur fracture reduction: Trajectory and force testing, in *2022 Int. Symp. Medical Robotics (ISMР)* (2022), pp. 1–6.
- M. S. Saeedi-Hosseiny, F. Alruwaili, S. McMillan, I. Iordachita and M. H. Abedin-Nasab, A surgical robotic system for long-bone fracture alignment: Prototyping and cadaver study, *IEEE Trans. Med. Robot. Bion.* **4**(1) (2022) 172–182, doi: 10.1109/TMRB.2021.3129277.
- K. Bouazza-Marouf, I. Browbank and J. R. Hewit, Robotic-assisted internal fixation of femoral fractures, *Proc. Inst. Mech. Eng. H. J. Eng. Med.* **209**(1) (1995) 51–58.
- B. Füchtmeier *et al.*, Reduction of femoral shaft fractures in vitro by a new developed reduction robot system 'RepoRobo', *Injury* **35** (2004) S-A113.
- K. Seide, M. Faschingbauer, M. E. Wenzl, N. Weinrich and C. Jürgens, A hexapod robot external fixator for computer assisted fracture reduction and deformity correction, *Int. J. Med. Robot. Comput. Assist. Surg.* **1**(1) (2004) 64, doi: 10.1581/mrcas.2004.010101.
- E. Rodr, A. P. Kypson, S. C. Moten, L. W. Nifong and W. R. C. Jr, A surgical telemanipulator for femur shaft fracture reduction, *Int. J. Med. Robot.* **2** (2006) 211–215, doi: 10.1002/rcs.
- M. Oszwald *et al.*, A rat model for evaluating physiological responses to femoral shaft fracture reduction using a surgical robot, *J. Orthop. Res.* **26**(12) (2008) 1656–1659.
- R. Westphal *et al.*, Robot-assisted long bone fracture reduction, *Int. J. Robot. Res.* **28**(10) (2009) 1259–1278, doi: 10.1177/0278364909101189.
- M. Oszwald *et al.*, Robot-assisted fracture reduction using three-dimensional intraoperative fracture visualization: An experimental study on human cadaver femora, *J. Orthopaedic Res.* **28**(9) (2010) 1240–1244.
- S. Wang, Y. Chen and Z. Ping, Control simulation of a six DOF parallel-serial robot for femur fracture reduction, in *Proc. 2009 IEEE Int. Conf. Virtual Environments, Human-Computer Interfaces, and Measurements Systems, VECIMS 2009* (IEEE, 2009), pp. 330–335, doi: 10.1109/VECIMS.2009.5068919.
- R. Ye and Y. Chen, Path planning for robot assisted femur shaft fracture reduction: A preliminary investigation, in *Proc. 2009 IEEE Int. Conf. Virtual Environments, Human-Computer Interfaces, and Measurements Systems, VECIMS 2009* (IEEE, 2009), pp. 113–117, doi: 10.1109/VECIMS.2009.5068876.
- R. Ye, Y. Chen and W. Yau, A simple and novel hybrid robotic system for robot-assisted femur fracture reduction, *Adv. Robot.* **26**(1–2) (2012) 83–104, doi: 10.1163/016918611X607383.
- L. Hu *et al.*, A femur fracture reduction method based on anatomy of the contralateral side, *Comput. Biol. Med.* **43**(7) (2013) 840–846, doi: 10.1016/j.combiomed.2013.04.009.
- P. Tang, L. Hu, H. Du, M. Gong and L. Zhang, Novel 3D hexapod computer-assisted orthopaedic surgery system for closed diaphyseal fracture reduction, *Int. J. Med. Robot. Comput. Assisted Surg.* **8**(1) (2012) 17–24.
- J. Wang, W. Han and H. Lin, Femoral fracture reduction with a parallel manipulator robot on a traction table, *Int. J. Med. Robot. Comput. Assist. Surg.* **9**(4) (2013) 464–471.
- T. Wang *et al.*, A removable hybrid robot system for long bone fracture reduction, *Biomed Mater Eng.* **24**(1) (2014) 501–509, doi: 10.3233/BME-130836.
- C. Li *et al.*, Accuracy analysis of a robot system for closed diaphyseal fracture reduction, *Int. J. Adv. Robot. Syst.* **11** (2014) 1–11, doi: 10.5772/59184.
- L. Hu, L. Zhang, R. U. S. A. Data, F. Application and P. Data, Long-bone fracture-reduction robot **2**(12) (2017).
- H. Du *et al.*, Advancing computer-assisted orthopaedic surgery using a hexapod device for closed diaphyseal fracture reduction, *Int. J. Med. Robot. Comput. Assist. Surg.* **11**(3) (2015) 348–359.
- C. Li *et al.*, A novel master-slave teleoperation robot system for diaphyseal fracture reduction: A preliminary study, *Comput. Assist. Surg.* **21** (2016) 163–168, doi: 10.1080/24699322.2016.1240304.

36. G. Dagnino, I. Georgilas, P. Köhler, R. Atkins and S. Dogramadzi, Image-based robotic system for enhanced minimally invasive intra-articular fracture surgeries, in *Proc. IEEE Int. Conf. Robot Autom.* 16–21 May 2016, Stockholm, Sweden, pp. 696–701, doi: 10.1109/ICRA.2016.7487196.
37. I. Georgilas, G. Dagnino, P. Tarassoli, R. Atkins and S. Dogramadzi, Robot-assisted fracture surgery: Surgical requirements and system design, *Ann Biomed. Eng.* **46**(10) (2018) 1637–1649, doi: 10.1007/s10439-018-2005-y.
38. G. Dagnino, I. Georgilas, P. Tarassoli, R. Atkins and S. Dogramadzi, Vision-based real-time position control of a semi-automated system for robot-assisted joint fracture surgery, *Int. J. Comput. Assist. Radiol. Surg.* **11**(3) (2016) 437–455, doi: 10.1007/s11548-015-1296-9.
39. G. Dagnino *et al.*, Image-guided surgical robotic system for percutaneous reduction of joint fractures, *Ann Biomed. Eng.* **45**(11) (2017) 2648–2662, doi: 10.1007/s10439-017-1901-x.
40. T. Essomba and S. Nguyen Phu, Kinematic analysis and design of a six-degrees of freedom 3-RRPS mechanism for bone reduction surgery, *J. Med. Dev.* **15**(1) (2021) 011101, doi: 10.1115/1.4049057.
41. P. K. Jamwal, S. Hussain and M. H. Ghayesh, Intrinsically compliant parallel robot for fractured femur reduction: Mechanism optimization and control, *Rob. Auton. Syst.* **141** (2021) 103787, doi: 10.1016/j.robot.2021.103787.
42. S. Lee *et al.*, 3D image-guided robotic system for bone fracture reduction, *IEEE Robot Autom. Lett.* **7**(2) (2022) 4353–4360, doi: 10.1109/LRA.2022.3150880.
43. W. Y. Kim, S. Joung, H. Park, J.-O. Park and S. Y. Ko, Human-robot-robot cooperative control using positioning robot and 1-DOF traction device for robot-assisted fracture reduction system, *Proc. Inst. Mech. Eng. H*, **236**(5) (2022), 697–710, doi: 10.1177/09544119221083140.
44. C. K. Yu, V. A. Singh, S. Mariapan and S. T. B. Chong, Antegrade versus retrograde locked intramedullary nailing for femoral fractures: which is better?, *Eur. J. Trauma Emerg. Surg.* **33**(2) (2007) 135–140.
45. S. S. Leonchuk, Lengthening of femur by combined osteosynthesis: A case report, *Med. Clin. Rev.* **3**(1) (2017) 12–14, doi: 10.21767/2471-299x.1000045.
46. M. Denisiuk and A. Afsari, Femoral shaft fractures, *StatPearls [Internet]* (2021).
47. R. Annappa, H. Mittal, S. U. Kamath, S. Rai, P. K. Suresh and N. Mohammed, Rotational malalignment after intramedullary fixation of trochanteric fractures, *J. Clin. Diagn. Res.* **12**(12) (2018) RC05–RC08, doi: 10.7860/JCDR/2018/34130.12357.
48. R. L. Jaarsma, D. F. M. Pakvis, N. Verdonchot, J. Biert and A. Van Kampen, Rotational malalignment after intramedullary nailing of femoral fractures, *J. Orthop. Trauma* **18**(7) (2004) 403–409.
49. J. W. Kim *et al.*, Malalignment after minimally invasive plate osteosynthesis in distal femoral fractures, *Injury* **48**(3) (2017) 751–757, doi: 10.1016/j.injury.2017.01.019.
50. O. Karaman, E. Ayhan, H. Kesmezacar, A. Seker, M. C. Unlu and O. Aydingoz, Rotational malalignment after closed intramedullary nailing of femoral shaft fractures and its influence on daily life, *Eur. J. Orthopaed. Surg. Traumatol.* **24**(7) (2014) 1243–1247, doi: 10.1007/s00590-013-1289-8.
51. M. Citak *et al.*, Femoral malrotation following intramedullary nailing in bilateral femoral shaft fractures, *Arch. Orthop. Trauma Surg.* **131**(6) (2011) 823–827, doi: 10.1007/s00402-010-1245-6.
52. Q. Zhu, B. Liang, X. Wang, X. Sun and L. Wang, Force-torque intraoperative measurements for femoral shaft fracture reduction, *Comput. Assist. Surg.* **21** (2016) 37–45, doi: 10.1080/24699322.2016.1240311.
53. T. Gösling *et al.*, Forces and torques during fracture reduction: Intraoperative measurements in the femur, *J. Orthopaed. Res.* **24**(3) (2006) 333–338.
54. L. S. Marchand, L. G. Jacobson, A. R. Stuart, J. M. Haller, T. F. Higgins and D. L. Rothberg, Assessing femoral rotation: A survey comparison of techniques, *J. Orthop. Trauma* **34**(3) (2020) e96–e101, doi: 10.1097/BOT.00000000000001648.
55. C. Zeckey *et al.*, Femoral malrotation after surgical treatment of femoral shaft fractures in children: A retrospective CT-based analysis, *Eur. J. Orthopaed. Surg. Traumatol.* **27**(8) (2017) 1157–1162, doi: 10.1007/s00590-017-1978-9.
56. C. de Boor, *A Practical Guide to Splines*, Vol. 27. (Springer-Verlag, New York, 1978).



**Fayeze Alruwaili** received B.S. and M.S. degrees in Biomedical Engineering from Wichita State University, Wichita, KS, USA, in 2018 and 2019, respectively. Fayeze is currently pursuing Ph.D. degree in Biomedical Engineering from Rowan University, Glassboro, NJ, USA. Fayeze's research interests include robotics, mechatronic systems, and haptic-human interaction.



**Marzieh S. Saeedi-Hosseiny** received her B.S. degree from College of Engineering at University of Tehran, Iran in 2008. She is currently a Ph.D. student in the Electrical and Computer Engineering Department and a research fellow in Surgical Robotics Lab at Rowan University. She is a co-author of three book chapters and multiple journal and conference papers. In 2020, she participated in NSF National I-Corps Program as an entrepreneurial lead. Her research interests are machine learning, image processing, computer vision, and surgical systems.



**Michael Clancy** received his B.Sc. in Bioengineering from the University of Pittsburgh and is currently a biomedical engineering Ph.D. student at Rowan University. His research interests include medical robotics, design and optimization of mechanisms, biomechanics, and signal processing.



**Sean McMillan** is a board certified orthopedic surgeon with specialty certification in orthopedic sports medicine (CAQ). He is the Chief of Orthopedics at the Virtua Health Willingboro and Camden Campuses and serves as the Director of Orthopedic Sports Medicine at Virtua Medical Group. Dr. McMillan lectures and teaches nationally and internationally on a variety of orthopedic sports medicine topics and is affiliated with the Rowan School of Osteopathic Medicine and Inspira Health orthopedic residencies. Dr. McMillan currently serves on the Board of Directors for the American Osteopathic Academy of Orthopedics (AOAO) as the second Vice President and is a past recipient of the AAOO Emerging Leader Award.



**Iulian I. Iordachita** received the M.Eng. degree in industrial robotics and the Ph.D. degree in mechanical engineering, from the University of Craiova, Craiova, Romania, in 1989 and 1996, respectively. In 2000, he was a Postdoctoral Fellow with the Brady Urological Institute, School of Medicine, Johns Hopkins University, Baltimore, USA, and in 2002-2003, he was a Research Fellow with the Graduate School of Frontier Sciences, The University of Tokyo, Tokyo, Japan. He is currently a Research Professor in mechanical engineering and robotics with the Johns Hopkins University, Baltimore, USA. His research interests include medical robotics, image guided surgery with a specific focus on microsurgery, interventional MRI, smart surgical tools, and medical instrumentation.



**Mohammad H. Abedin-Nasab** received his M.S. and Ph.D. degrees in mechanical engineering from Sharif University of Technology in 2006 and 2012, respectively. He is currently an Assistant Professor and the Director of Surgical Robotics Lab at Rowan University in New Jersey. He is also the Editor of the Handbook of Robotic and Image-Guided Surgery. Dr. Abedin-Nasab specializes in surgical robotics, robotics, biomechanics, and nonlinear modeling. He has focused on both basic and applied research endeavors, ensuring that his research is consistently relevant to the scientific community as well as the health-care system and medical robotics industry.